A Three-Dimensional Registration Method for Automated Fusion of Micro PET-CT-SPECT Whole-Body Images

Meei-Ling Jan, *Member, IEEE*, Keh-Shih Chuang*, Guo-Wei Chen, Yu-Ching Ni, Sharon Chen, Chih-Hsien Chang, Jay Wu, Te-Wei Lee, and Ying-Kai Fu

***Abstract*—Micro positron emission tomography (PET) and micro single-photon emission computed tomography (SPECT), used for imaging small animals, have become essential tools in developing new pharmaceuticals and can be used, among other things, to test new therapeutic approaches in animal models of human disease, as well as to image gene expression. These imaging techniques can be used noninvasively in both detection and quantification. However, functional images provide little information on the structure of tissues and organs, which makes the localization of lesions difficult. Image fusion techniques can be exploited to map the functional images to structural images, such as X-ray computed tomography (CT), to support target identification and to facilitate the interpretation of PET or SPECT studies. Furthermore, the mapping of two functional images of SPECT and PET on a structural CT image can be beneficial for those in vivo studies that require two biological processes to be monitored simultaneously. This paper proposes an automated method for registering PET, CT, and SPECT images for small animals. A calibration phantom and a holder were used to determine the relationship among three-dimensional fields of view of various modalities. The holder was arranged in fixed positions on the couches of the scanners, and the spatial transformation matrix between the modalities was held unchanged. As long as objects were scanned together with the holder, the predetermined matrix could register the acquired tomograms from different modalities, independently of the imaged objects. In this work, the PET scan was performed by Concorde's microPET R4 scanner, and the SPECT and CT data were obtained using the Gamma Medica's X-SPECT/CT system. Fusion studies on phantoms and animals have been successfully performed using this method. For microPET-CT fusion, the maximum registration errors were 0.21 mm $\pm$ 0.14 mm, 0.26 mm $\pm$ 0.14 mm, and 0.45 mm $\pm$ 0.34 mm in the X (right-left), Y (upper lower), and Z (rostral-caudal) directions, respectively; for the microPET-SPECT fusion, they were 0.24 mm $\pm$ 0.14 mm, 0.28 mm $\pm$ 0.15 mm, and 0.54 mm $\pm$ 0.35 mm in the X, Y, and Z directions, respectively. The results indicate that this simple method can be used in routine fusion studies.**

***Index Terms*—Image fusion, micro computed tomography (CT), micro positron emission tomography (PET), micro single-photon emission computed tomography (SPECT), registration.**

I. Introduction

NONINVASIVE technologies that image various aspects of the disease process for clinical diagnosis are divided into two types—structural and functional images. X-ray computed tomography (CT) and magnetic resonance (MR) imaging provide mainly high-resolution images with anatomical information, whereas single-photon emission computed tomography (SPECT) and positron emission tomography (PET) provide functional information, but with coarser resolution. Fusing these two types of images solves the problem of the insufficiency of the information provided by a single modality. In recent years, the success of PET-CT imaging in the clinical field has triggered substantial interest in noninvasive molecular and anatomical imaging of small laboratory animals. The limited spatial resolution and high specificity of imaging probes have often enabled little morphologic information to be obtained from micro PET or micro SPECT images, making molecular investigations difficult to interpret [1]. Integrating anatomical and functional tomographic datasets to improve both qualitative detection and quantitative determination in small animal molecular investigations is expected to provide much more information.

The integration is achieved in two stages: the first is to derive the geometric transformation between the two three-dimensional (3-D) datasets (known as registration) and the second is to fuse the images by generating a single image from the two registered originals. The registration procedure comprises three separate processes—identification, matching, and verification. The identification process is the isolation of features that can be directly compared. The matching process compares the features of images from both modalities and computes the optimal transformation between the two datasets. Matching is formulated as the minimization of a cost function, which measures the difference between the two sets of features being identified. A final visual check must be performed for confirmation.

Manuscript received December 15, 2004; revised March 4, 2005. This work was supported in part by the National Science Council, Taiwan, R.O.C., under Grant NSC93-2623-7-007-015-NU. The work of K.-S. Chuang was supported by the Medical Research Advancement Foundation under Joint Grant VGHTH 87-26-3. The Associate Editor responsible for coordinating the review of this paper and recommending its publication was R. Jaszczak. *Asterisk indicates corresponding author.*

M.-L. Jan is with the Institute of Nuclear Energy Research, Longtan, Taiwan 32546, R.O.C. She is also with the Department of Nuclear Science, National Tsing-Hua University, Hsinchu, Taiwan 30043, R.O.C. (e-mail: mljan@iner.gov.tw).

*K.-S. Chuang is with the Department of Nuclear Science, National Tsing-Hua University, Hsinchu, Taiwan 30013, R.O.C. (e-mail: kschuang@mx.nthu.edu.tw).

G.-W. Chen, Y.-C. Ni, C.-H. Chang, T.-W. Lee, and Y.-K. Fu are with the Institute of Nuclear Energy Research, LongTan, Taiwan 32546, R.O.C.

S. Chen and J. Wu are with the Department of Nuclear Science, National Tsing-Hua University, Hsinchu, Taiwan 30013, R.O.C.

Digital Object Identifier 10.1109/TMI.2005.848617

Image registration must consider variations in an object's positioning among different scans. For instance, the actual orientation and the section center, in relation to the object's anatomy, are hard to keep the same for each scan. Moreover, the imaging parameters such as section thickness, matrix size, pixel size, and intersection gap are subject to the scanner's limitations. To register images from different modalities, geometric transformation that incorporates translation, rotation, and scaling of the datasets is suggested to be found. Various methods have been proposed for finding the geometric transformation of different imaging modalities [2], including, for example, headholder alignment [3], external fiducial alignment [4], stereotaxic frames [5], [6], and internal landmark matching [7]. The first three methods use external markers attached to the object's skin or face and cannot be used in a retrospective study if no markers are applied in the experiment. The stereotaxic frames method is the most accurate means of localization, but the invasiveness of the frame limits its use. A more flexible way to accomplish registration is to consider anatomical features visible in the tomograms from each modality [8]. This method has the potential for higher registration accuracy than the use of external markers and involves less interference with normal radiographic procedures.

All of these methods have been developed for human studies. Therefore, when applied to studies in animals, which are much smaller than humans, the number of suitable features is limited, and the features are commonly difficult to locate. Little is known about the performance in small animals of image registration algorithms that are effective in human studies [9]. Stout *et al.* [10] employed small-bore Teflon tubing filled with black ink and F-18 as a marker and attached it to a wooden framework to register the image. Although their goal was to generate a stereotactic mouse atlas, their method can also be used in fusion studies. Vaquero *et al.* [11] used external fiducial markers to evaluate the capability of the automated image registration and mutual information algorithms to register PET images of the rat skull and brain to CT or MR images of the same animal. They concluded that the mutual information algorithm appears to be a robust method for registering PET, CT, and MR images of the rat head. However, the mutual information algorithm requires manual prealignment and volume trimming before registration.

The aim of this was to develop an automatic method for registering small animal images. A calibration phantom and a holder were designed to obtain the relationship among three-dimensional fields of view of independent modalities. Animals were secured to the holder, which was arranged at fixed locations on the couches of scanners to determine the spatial transformation matrix between modalities. If the position of the holder remains the same, the predetermined matrix can register the acquired tomograms from different modalities automatically and independently of the imaged object. The geometric transformation between different modalities is simply a linear function approximation problem, which can be solved using linear polynomial regression. The coordinates of the markers in a calibration phantom from both modalities are used to determine the transformation matrix between the two modalities. After the geometric relationship of the two modalities has been derived, each voxel value of the desired image can be identified by mapping its coordinates.

II. Material and Methods

A. Rigid Body Transformation

The acquired tomograms were assumed to be related by a rigid body transformation. Any given 3-D position vector pairs $\{\mathbf{p}_i\}$ and $\{\mathbf{p}'_i\}$, where $i = 1, \ldots, n$, and n is the number of voxels, are related by

$$\mathbf{p}'_i = \mathbf{s}\mathbf{R}\mathbf{p}_i + \mathbf{T} \tag{1}$$

where $\mathbf{s}$ and $\mathbf{R}$ are 3×3 scaling and rotation matrices and $\mathbf{T}$ is a translation vector (3×1). The objective of registration is to find $\mathbf{s}$, $\mathbf{R}$, and $\mathbf{T}$ such that the sum of squared errors (SSE), given by

$$\text{SSE} = \sum_{i=1}^{n} \left|\mathbf{p}'_i - (\mathbf{s}\mathbf{R}\mathbf{p}_i + \mathbf{T})\right|^2 \tag{2}$$

is minimized.

The relationship between $\mathbf{p} = (x, y, z)^t$ and $\mathbf{p}' = (x', y', z')^t$, where superscript t represents matrix transposition, can be estimated according to a polynomial equation

$$\begin{aligned} x' &= a_{00} + a_{01}x + a_{02}y + a_{03}z + a_{04}xy + a_{05}xz + a_{06}yz \\ y' &= a_{10} + a_{11}x + a_{12}y + a_{13}z + a_{14}xy + a_{15}xz + a_{16}yz \\ z' &= a_{20} + a_{21}x + a_{22}y + a_{23}z + a_{24}xy + a_{25}xz + a_{26}yz. \end{aligned}$$

The a_{ij} values can be determined by differentiating the SSE with respect to a_{ij} and equating the results to zero to generate a set of normal equations in matrix form $\mathbf{X}\mathbf{A} = \mathbf{g}$, such that

$$\mathbf{X} = \begin{bmatrix} n & \sum_{i=1}^{n} x_i & \sum_{i=1}^{n} y_i & \cdots & \sum_{i=1}^{n} y_i z_i \\ \sum_{i=1}^{n} x_i & \sum_{i=1}^{n} x_i^2 & \sum_{i=1}^{n} x_i y_i & & \vdots \\ \vdots & \vdots & \vdots & & \vdots \\ \sum_{i=1}^{n} y_i z_i & \sum_{i=1}^{n} x_i y_i z_i & & \cdots & \sum_{i=1}^{n} y_i^2 z_i^2 \end{bmatrix}$$

$$\mathbf{g} = \begin{bmatrix} \sum_{i=1}^{n} x'_i & \sum_{i=1}^{n} y'_i & \sum_{i=1}^{n} z'_i \\ \sum_{i=1}^{n} x_i x'_i & \sum_{i=1}^{n} x_i y'_i & \sum_{i=1}^{n} x_i z'_i \\ \vdots & \vdots & \vdots \\ \sum_{i=1}^{n} y_i z_i x'_i & \sum_{i=1}^{n} y_i z_i y'_i & \sum_{i=1}^{n} y_i z_i z'_i \end{bmatrix} \tag{3}$$

and

$$\mathbf{A} = \begin{bmatrix} a_{00} & a_{10} & a_{20} \\ a_{01} & a_{11} & a_{21} \\ \vdots & \vdots & \vdots \\ a_{06} & a_{16} & a_{26} \end{bmatrix}$$

hold. $\mathbf{X}$ and $\mathbf{g}$ were derived from the coordinates of the corresponding markers in the calibration phantom tomograms from different modalities. These equations were then solved to determine $\mathbf{A}$ by matrix inversion using Gauss–Jordan elimination.

B. Scanners for Micro PET, Micro CT, and Micro SPECT Imaging

Micro CT images were obtained using an X-SPECT/CT animal imaging system (Gamma Medica, Northridge, CA). This was the first commercially available, dual modality, SPECT and X-ray CT system for imaging animals in medical research. The micro CT element of the X-SPECT/CT system comprised a micro focus X-ray tube and a flat-panel X-ray detector. The X-ray source was a fixed anode tube with 250 μm spot size. The flat-panel detector was a 120-mm gadolinium oxysulfide/CMOS detector with 50 μm pitch size. The animals were positioned horizontally on a stationary bed and the X-ray tube was rotated around the subjects. The distance from the X-ray tube to detector was 298.0 mm, and the distance from the X-ray tube to center of rotation was 225.0 mm. The operating current and voltage of the X-ray tube were set to 0.5 mA and 50 kVp, respectively. Each scan had 256 projections with a 0.5-s exposure per projection. Tomograms were reconstructed by applying the Feldkamp algorithm [12] on a volume of $512 \times 512 \times 512$ voxels with isotropic 0.15-mm voxel size.

The compact gamma camera used in X-SPECT was based on pixilated NaI(Tl) scintillators in combination with a position-sensitive photomultiplier tube readout. The scintillator array had a 58×58 matrix of $2 \times 2 \times 6$ mm^3 crystals. Two gamma cameras were mounted 180° opposite the axis of rotation. Various interchangeable pinhole and parallel-hole collimators, with various hole-sizes, ranging from 0.5 to 2.0 mm, were used to optimize the resolution, the sensitivity and the field of view for particular applications. The projections were reconstructed using ordered subsets expectation maximization reconstruction software [13]. For the X-SPECT/CT system, the object in the fusion study did not move, and the registration was performed using built-in spatial transformation. After registration, both the SPECT and the CT tomograms had $256 \times 256 \times 256$ voxels in an isotropic 0.3-mm voxel size.

The PET data were obtained with a microPET R4 system (Concorde Microsystems, Knoxville, TN). The detector material of the scanner models was lutetium oxyorthosilicate (CTI, Knoxville, TN), with dimensions of $2.1 \times 2.1 \times 10$ mm^3 and a center-to-center distance of 2.4 mm, providing a spatial resolution of around 2 mm at the center of the tomogram [14]. For all measurements, a coincident time window of 6 ns and an energy window of 350–650 keV were used. After data histogramming, 3-D sinogram datasets were reconstructed by 3-D reprojection [15], yielding a tomogram with $256 \times 256 \times 63$ voxels. The voxel size of the images was $0.25 \times 0.25 \times 1.22$ mm^3.

C. Designing the Animal Holder and Calibration Phantom

An animal holder and a calibration phantom were designed for registration to determine the spatial relation between the microPET and X-SPECT/CT datasets. The 80-mm-wide 200-mm-long holder (Fig. 1) was used to transfer the object between systems. Alignment markers on both sides of the couch helped to place the holder at a fixed position in each scan. A bull-eye spirit level was mounted on the holder to improve further the precision of the positioning. While the holder was in position, the spatial relation between the images of these two modalities was fixed and its transformation matrix remained constant.

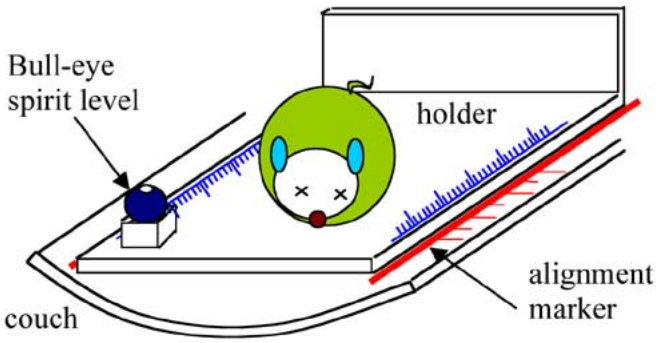

Fig. 1. Animal holder was aligned with the markers on the couch. A bull-eye spirit level was mounted on top of the holder to improve the precision of the positioning.

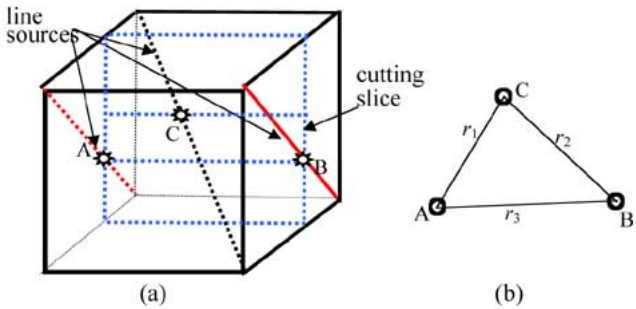

Fig. 2. (a) The calibration phantom consisted of three line sources A, B, and C. (b) A typical transaxial slice of the phantom images showed three bright spots that can be identified as the positions of markers. Notably, source C is always located between A and B. Let r_1, r_2, and r_3 be the distances between the markers AC, BC, and AB, respectively. The ratios of these parameters are used to find the corresponding markers in the target dataset.

To obtain the transformation matrices between the PET and CT modalities, a calibration phantom placed on the holder was scanned by the two scanners. The method assumes a rigid body transformation. Although theoretically, three point markers would provide a simpler method of uniquely determining the transformation matrix, the limited resolution of images was such that determining the exact locations of the matched markers was not ensured. Errors arise will be introduced in the estimation of both $\mathbf{p}$ and $\mathbf{p}'$ and, therefore, in the transformation matrix. More markers are required to reduce these errors. Hill *et al.* [2] revealed that the target registration error decreases as $1\sqrt{N}$, where N is the number of point markers. In this paper, three-line sources for 39 markers are used to determine the transformation matrix. Placing three line sources as 39 markers would be much easier and more practical than placing 39 point-source markers. The calibration holder consisted of three glass capillary tubes with an inner diameter of 1 mm and a length of 100 mm that were placed on an acrylic housing. These three capillaries were filled with [^{18}F]2-deoxy-2-fluoro-D-glucose ([^{18}F]-FDG) solution, which appeared as bright spots in the transaxial image of the PET output. The three capillaries were arranged [Fig. 2(a)] to maximize the spatial separations between each other and the central capillary (C) was positioned between two side capillaries (A and B). The capillaries appeared as white circles in the transaxial slices of CT image and their centers were used to register spots in PET images. The centers of the three capillaries crossing selected

slices in the reference image were located [Fig. 2(b)] and two position parameters ($t_1 = r_1/r_3, t_2 = r_2/r_3$) were calculated. The parameters (t_1, t_2) were using to determine the corresponding markers in target image. Registration between SPECT and CT is already provided for Gamma Medica's X-SPECT/CT scanner, so PET-SPECT fusion was also achieved with reference to CT images after SPECT-CT registration.

D. Transformation Matrix

In this paper, PET images were selected as the reference dataset. Thirteen equally spaced PET slices (uniformly distributed between $z = 1, 63$) were selected, and the locations of three capillaries of these slices were used as the reference markers. A total of 39 markers were therefore divided into 13 groups of three markers each. All the coordinates of the markers could be determined for each selected slice in the PET images. These markers in each group in CT were located using the following method. Let $\mathbf{p}_i$, $i = 1, 2, 3$ be the coordinates of the three markers (from left to right) on the same slice ($z_1 = z_2 = z_3 = z$); their corresponding locations, $\mathbf{p}'_i$, $i = 1, 2, 3$, in the CT images are then determined. (Their z coordinates z'_1, z'_2, z'_3 are not necessarily the same.) A two-step process was employed to solve for $\mathbf{p}'_i$. An initial guess that z'_1, z'_2, and z'_3 were equal to z'_c was made, and the central capillary was located at $\mathbf{p}'_2$ between two side capillaries. The slice z'_c was easily found using the distance ratio as a criterion, such that Err$= (t_1 - t'_1)^2 + (t_2 - t'_2)^2$ is minimal, where t_1, t_2 and t'_1, t'_2 are the position parameters measured from the capillary locations in the PET and CT images, respectively. The second step was to search for $\mathbf{p}'_i$ again using the distance ratio as a criterion within slices $z'_c \pm \Delta z$, where Δz is selected arbitrarily, but should be sufficiently large to cover possible errors in the placing of the holder. The markers of the other 12 groups were located using the same two-step process. The coordinates of these 39 matched markers were then used to calculate the transformation matrix for PET-CT fusion. The same method was applied to the SPECT datasets (after SPECT-CT registration in the Gamma Medica system) for PET-SPECT fusion.

After the holder had been calibrated, registration was performed for animal studies. Anesthetized animals were secured to the holder to prevent movement during scanning. The holder, together with the animals, was carefully positioned on the couches for PET, CT, and SPECT scanning. The transformation matrices determined by scanning the holder and the calibration phantom enabled the spatial relationship among modalities to be interpolated for animal locations in SPECT, CT and PET scanners. Following scanning, the CT or SPECT images were transformed into the PET coordinate system. This was achieved by scanning all voxels of the PET datasets and locating the corresponding voxels in the CT dataset using (3). After the transformation had been performed, a transparent overlay of images of one modality on the other was generated for evaluation, each with different color lookup tables. Fig. 3 presents a flowchart of this method.

III. Results

Fig. 4 plots the coordinates of the locations of markers from the images of the calibration phantom, as well as the coordinates calculated using the transformation matrix. The markers of both CT and PET in the fusion images were visually checked and their registrations found to agree with each other closely. The average SSE of the regression was 0.11 voxels. Notably, the quality of the Feldkamp algorithm varies with the elevation of the plane [12], [16]. For slices farther away from the central plane, blurring in the axial direction occurs. The blurring causes the exact positions of the markers to be difficult to identify. Therefore, about ten slices in the front and end sections of the CT images were not used in the registration study.

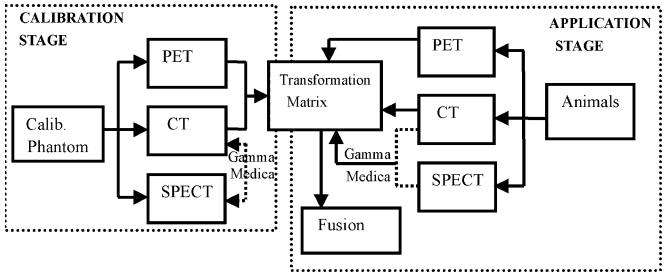

Fig. 3. Flowchart of proposed registration method.

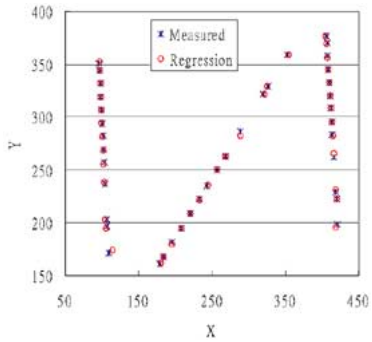

Fig. 4. Regression results concerning source positions (x, y) in the calibration phantom. The z coordinates of the source locations were projected onto the X-Y plane shown here.

The registration errors of this method come primarily from the uncertainty in the alignment of the holder. The calibration phantom together with the holder were repositioned at the same location seven times for both CT and PET scanning to estimate the holder-alignment errors. Position parameters (described in Section II-D) of nine markers on three slices ($Z_{\mathrm{PET}} = 7, 31, 54$) of a PET image were selected to evaluate holder-alignment errors among PET scans. The selected slices represent three axial regions (rostral, central, and caudal) of the images. The nine corresponding markers with the same position parameters in the other six PET images were located. Fixed position parameters that corresponded to $Z_{\mathrm{CT}} = 62, 256, 450$ were selected, and the same procedure as PET was followed, to assess holder-alignment errors among CT scans. Table I presents the means and standard deviations of three repositioned central markers (C) for CT and PET. The deviations of these nine repositioned markers reveal that the holder-alignment errors associated with PET and CT are smaller than one voxel, except that of CT in the Z-direction, because the couch of CT has no sensor. Therefore, the motions of the couch into scanned position were checked visually.

Registration errors were evaluated for various positional setups for both PET and CT scans to test the robustness of

TABLE I
HOLDER-ALIGNMENT ERRORS AMONG PET AND CT SCANS

MICRO PET

X (Unit: Voxel $_{PET,X}$)	Y (Unit: Voxel $_{PET,Y}$)	Z (Unit: Voxel $_{PET,Z}$)
98.99±0.37	146.34±0.40	6.57±0.53
122.07±0.37	122.17±0.52	30.71±0.49
144.58±0.13	98.47±0.20	54.29±0.49

MICRO CT

X (Unit: Voxel $_{CT,X}$)	Y (Unit: Voxel $_{CT,Y}$)	Z (Unit: Voxel $_{CT,Z}$)
178.25±0.20	308.59±0.30	61.57±1.40
247.33±0.22	246.36±0.21	256.29±1.80
316.08±0.12	184.90±0.13	449.86±1.68

the system. Again, the calibration phantom and the holder assembly were randomly repositioned, but not beyond the field of view, seven times for PET scans. The same procedure was followed for CT scans. Selecting the locations of the capillaries in PET as the reference markers enabled the corresponding positions in CT to be obtained either by the transformation matrix or by the minimum position parameters method. In these studies, $\mathbf{p}'_{ijk}$ and $\mathbf{p}''_{ijk}$, $i = 1, 2, \ldots, 7$, $j = 1, 2, \ldots, 7$, $k = 1, 2, \ldots, 39$, were the coordinates of the kth marker in CT, obtained by the minimum position parameters method using the ith CT and the jth PET pairs, and using the ith transformation matrix associated with the jth PET image, respectively. The registration accuracy (E_i) in the ith study is defined as the maximum Euclidean distance difference of any pair of the 39 coordinates of the markers for all seven PET images: $E_i = \max_j \max_k |\mathbf{p}'_{ijk} - \mathbf{p}''_{ijk}|$.

Fig. 5 shows the procedure for evaluating the registration error in each CT study. The average registration errors in these studies were 0.21 mm ± 0.14 mm, 0.26 mm ± 0.14 mm, and 0.45 mm ± 0.34 mm, in the X (right–left), Y (upper–lower) and Z (rostral–caudal) directions, respectively, for PET-CT fusion. The same method was applied to the PET-SPECT fusion study, and the registration errors were 0.24 mm ± 0.14 mm, 0.28 mm ± 0.15 mm, and 0.54 mm ± 0.35 mm, along the X, Y, and Z axes, respectively. These small registration errors indicate that this method was quite robust. The registration error is higher in the Z direction than in either the X or the Y directions, because the holder-alignment error of CT is the highest along the Z axis, and the resolution of PET is the lowest along the Z axis. Regression relationships are valid only for values of the regressor variable in the range of the original data. If the object is outside the range of the calibration phantom, then extrapolations from the regression variable deteriorate the image. In such a case, a larger calibration phantom that covers the entire field of view is required.

A Derenzo-like phantom was used to confirm this method. The phantom consisted of hot rods of various sizes (1.2-, 1.6-, 2.4-, 3.2-, 4.0-, and 4.8-mm diameter) arranged in six groups. The spacing between adjacent rods in each group was twice the rod diameter. The phantom was 40.0 mm in diameter and 36.0 mm in length. The Derenzo-like phantom was filled with 11.4 MBq [^{18}F]-FDG and KI solution for easy visualization by both PET and CT. The phantom was taped tightly onto the holder. After a 10-min PET scan, the phantom and the holder together were moved to the CT couch to undergo another 10-min scan. Fig. 6 presents typical transaxial and coronal slices of registered CT, PET, and fusion images from the phantom dataset. The fusion images show the close match between the locations of the hot spots on both images.

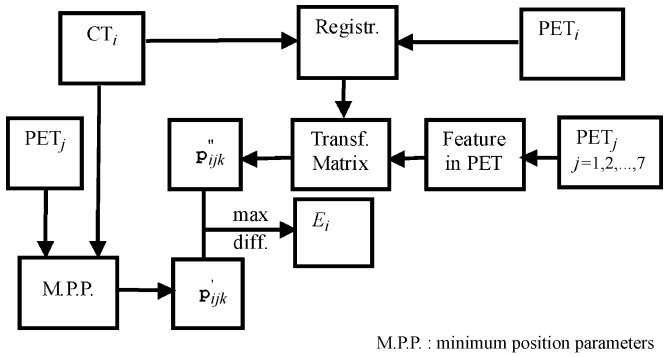

Fig. 5. Procedure for calculating registration error in the fusion study. The procedure was repeated for $i = 1, 2, \ldots, 7$.

A seven-week-old male C57BL/6 mouse was injected intravenously with Lewis lung carcinoma cells (LLC1) 16 days before imaging. After 16 days, the mouse, now with tumors and weighing 19.5 g, was injected with 9.8 MBq [^{18}F]-FDG and scanned by PET for 10 min from the time of injection, in a single bed position. After the first PET scan, the mouse, together with the holder, was shifted to the CT modality for a 10-min CT scan. When the CT scan was finished, the mouse was transferred back to the PET scanner for another 10-min PET scan. The second-step PET scan was begun at 60 min after injection. After all PET and CT scans had been completed, the mouse was sacrificed and the lungs and liver biopsied. For comparison, a fusion study was conducted on a 22.0 g normal C57BL/6 mouse injected with 9.4 MBq [^{18}F]-FDG. After 60 min of uptake, the mouse underwent a PET scan (10 min scan time) and a CT scan (10 min scan time). Both the normal mouse and the mouse with tumors were anaesthetized by intravenously injecting suitable anesthetics through the tail vein to prevent motion during the PET and CT scans. The animal experiments were approved by the Institutional Animal Care and Use Committee at the Institute of Nuclear Energy Research in Taiwan.

Fig. 7 displays selected coronal slices from the registered CT and the 60 min [^{18}F]-FDG uptake PET datasets of the mouse with tumors. Tumors in the lungs can be clearly interpreted with the help of anatomic information from CT images. Comparing Fig. 7 with the results of PET-CT registration of the normal mouse (Fig. 8) clearly shows that no [^{18}F]-FDG was taken up in the ribcage of the normal mouse, except in the heart. Tumors were present not only in the lungs but also in the liver (Fig. 7). The CT images without using contrast agent did not clearly show the precise location of the liver, so the tumors in the liver were identified by images obtained from the two-step PET scans. Fig. 9(a) and (b) shows the two PET images, representing the first-step (0–10 min) and second-step (60–70 min)

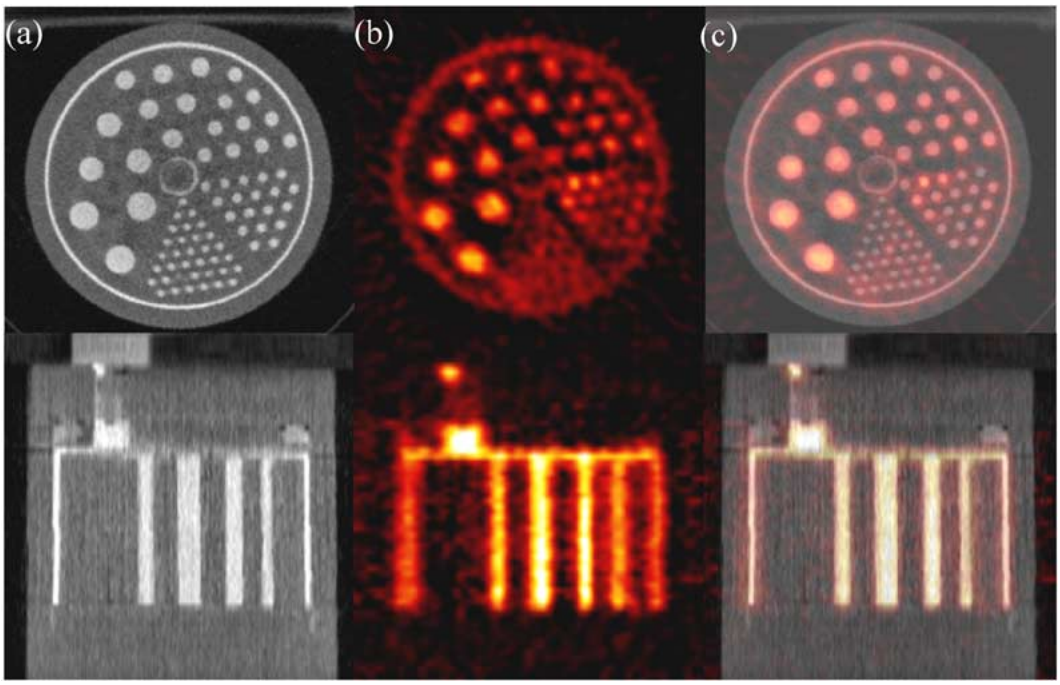

Fig. 6. (Top) Transaxial slices and (bottom) coronal slices of registered (a) CT, (b) PET, and (c) fused images of the Derenzo-like phantom. The hot-rod diameters in each of the six sectors are 4.8, 4.0, 3.2, 2.4, 1.6, and 1.2 mm. Notably, the hot spots (PET) fit well the outlines of the bright rods (CT).

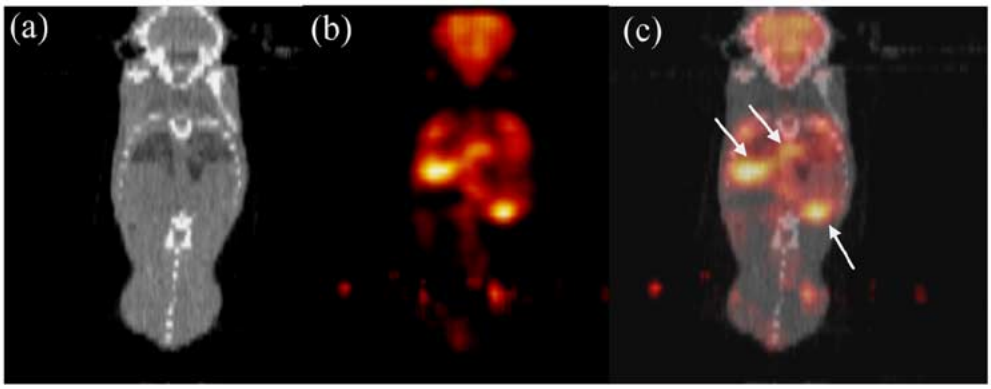

Fig. 7. (a) Anatomic information of a mouse obtained from CT. (b) Coronal slice displays the uptake of [^{18}F]-FDG in the mouse 1 h after injection. (c) The locations of tumors (arrows) were identified with the help of anatomic information.

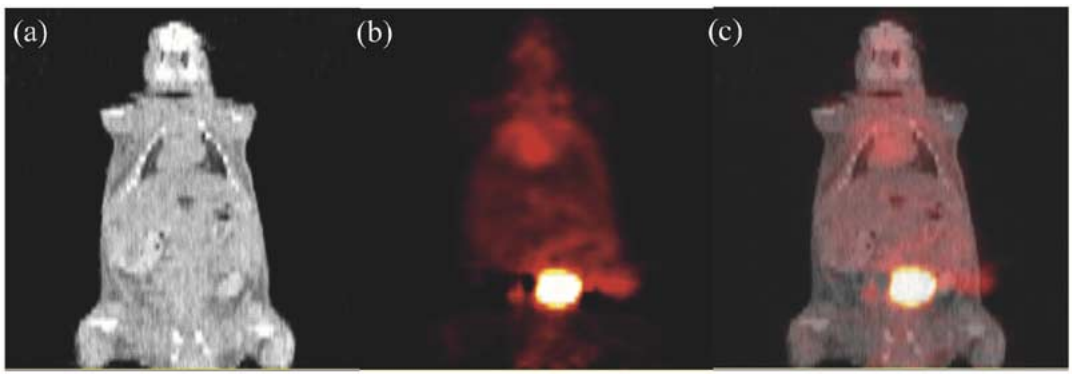

Fig. 8. Spatially registered coronal (a) CT and (b) PET images of a normal C57BL/6 mouse and (c) fused image. The ribcage exhibits no special [^{18}F]-FDG uptake except in the heart.

[^{18}F]-FDG metabolic distributions of the mouse the same as in Fig. 7, respectively. Notably, the registration between these two PET images remained accurate even though the mouse underwent CT scanning between these two PET studies. The liver can be resolved in the first-step PET images, but it was hardly visible in the second-step PET images. The [^{18}F]-FDG uptake of

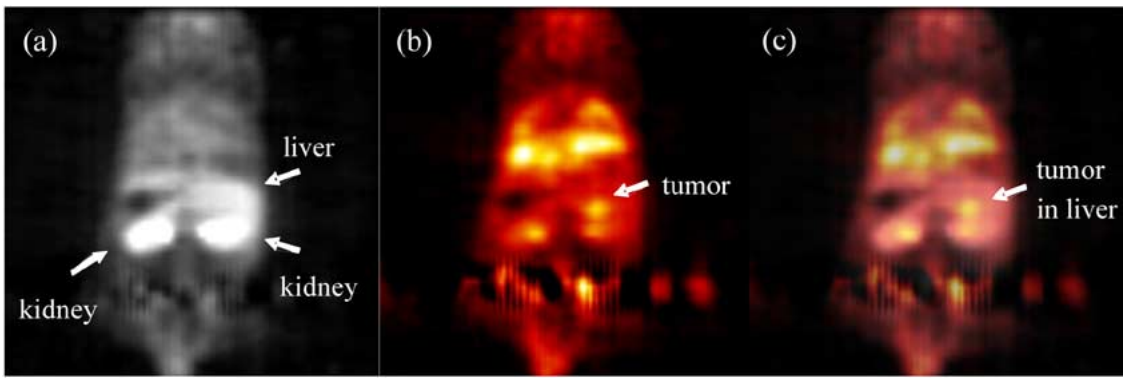

Fig. 9. Spatially registered, coronal, two-step PET images of a C57BL/6 mouse with Lewis lung carcinoma. (a) and (b) present the [^{18}F]-FDG uptake distributions of the mouse from 0 to 10 min and from 60 to 70 min after injection. (c) Fused two-step PET images can help to locate the tumor in the liver.

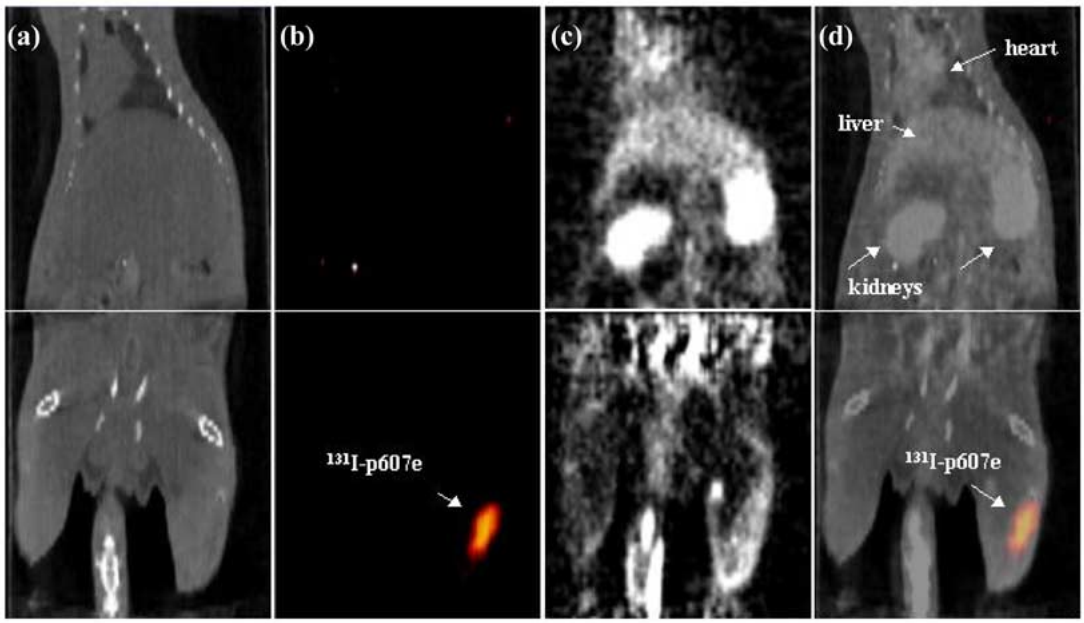

Fig. 10. (a) CT, (b) SPECT, and (c) PET coronal images of the (top) abdominal region and (bottom) legs of a rat. (d) The fused image of the three modalities clearly resolves the heart, chest, ribs, liver, and kidneys, as well as the bright spot ([^{131}I]-p607e) in the right leg. Most of the [^{131}I]-p607e remained in the initial position for 14 days and remained away from the heart, liver, and kidneys.

the normal liver was washed out rapidly, except where tumors were present. Fig. 9(c) displays the superimposed PET images, from which the location of the tumor (arrow) can be identified in the liver. The tumors in the lungs and liver were confirmed by microscopic examination after the study.

An adult Sprague–Dawley rat that weighed 650 g was injected with both I-131 and F-18 and scanned to perform fusion of the three modalities (PET-SPECT-CT). The rat was injected with 9.25 MBq [^{131}I]-p607e 14 days before the SPECT scan. The [^{131}I]-p607e peptide, combined with an oil-based adjuvant, was used as a water-in-oil emulsion and was injected intramuscularly into the right leg of the rat to assay for stability. Medium-energy pinhole collimators were used in this imaging. The scan time was 80 min/bed $\times$ 2 bed positions for 32 projections/bed, and was followed by CT scans of 10 min/bed $\times$ 2 bed positions. The rotational center-to-aperture distance was set to 32.7 mm, corresponding to a 92.4 mm field of view. The rat and the holder were transferred to the PET couch after the SPECT and CT scans had been completed. A 10 min PET scan centered on the rat's abdomen was started immediately after 16.65 MBq [^{18}F]-FDG was injected through the tail vein. The second 10 min PET scan was focused on the legs and was begun immediately after the first bed scan was completed. The SPECT, CT, and PET tomograms were reconstructed separately. Both the SPECT and CT reconstructed images were registered using software provided by Gamma Medica. Two datasets with $256 \times 256 \times 256$ voxels were obtained after registration. The method described above was then used to perform the PET-CT and PET-SPECT registrations.

Fig. 10(a)–(c) presents CT, SPECT, and PET coronal images, respectively, of the (top) abdominal region and (bottom) legs of the rat. Fig. 10(d) shows fused images of the three modalities. The three-modality image, displayed in the upper panel of Fig. 10(d), clearly presents the heart, chest, ribs, liver, and kidneys; the red spot [lower panel of Fig. 10(d)] in the right leg is the [^{131}I]-p607e that had been injected 14 days before scanning. The fusion images of the PET-SPECT-CT modalities indicate that most of the [^{131}I]-p607e remained in the initial position and was kept away from the heart, liver, and kidneys.

IV. Discussion

Interest is growing in multimodality fusion in investigations of small experimental animals. For such investigations, methods must be devised by which the results of each modality can be interpreted with reference to those of the other modalities at every point in their conjoint imaging space. Registration algorithms based on internal or external markers enable accurate image registration that is not based on assumptions concerning image content. The small size of animals and the limited resolution of the PET system are such that the images do not always clearly show the internal markers, and user involvement is required to identify these markers. The use of external markers depends on a complex setup in each study, and the transformation matrices required for various objects must be recalibrated each time. The external fiducial markers might be unreliable in image registration. The skin position of the external markers does not correlate well with the body frame because skin has large freedom of motion. Moreover, external markers can interfere with the experimental design and have other practical shortcomings; for example, attaching them rigidly to a living animal can be difficult. The method presented herein considers the holder as an external frame, and this does not interfere with any experimental design. The fusion work can be performed on any part of the imaged body. The transformation matrix is the same for animal studies, as long as the scanning holder is placed at fixed locations. Therefore, the images acquired from various modalities can be registered automatically using the predetermined matrix, independently of the imaged object. The proposed method can be used to perform fusion studies between any two modalities. For instance, if capillaries of the calibration phantom are filled with MR contrast agent, then multimodality studies including MRI can be undertaken as well. This method is also appropriate for making simultaneous multianimal comparisons, as long as the scanning holder and calibration phantom are large enough.

The registration accuracy depends strongly on the transformation matrix. The transformation matrix is determined from the scanned datasets of the calibration phantom with the holder. The preparation of the calibration phantom including the three-line sources is simple and fast. In this study, 39 markers were employed to determine the transformation matrix. To place three-line sources for 39 markers would be much easier and more practical than to place 39 point-source markers. The markers of the phantom were easy to identify, so no physician is required to assess the registration. The calibration procedure is fully automatic and involves no user intervention. The coordinates using the transformation matrix must be calculated without extrapolation to minimize the registration error. Therefore, the calibration phantom should be made as large as possible to fit the field of view of the scanners, and the markers of the calibration phantom would cover the full range of the scanned object to achieve accurate registrations in three dimensions. The performance of this registration method is independent of the quality of the CT, PET, and SPECT images. Neither the tissue contrast nor the statistical quality of the PET and SPECT images influences the registration accuracy, except in the imaging of the calibration phantom to determine the transformation matrix. The animals require no special preparation before imaging, and no extra optimal data processing is required following imaging, so this registration method is effective for routine fusion studies.

V. Conclusion

We have developed an automated registration method for animal imaging among micro PET, micro CT, and micro SPECT modalities that does not interfere in any way with normal image acquisition. The predetermined transformation matrix, which specifies the spatial relationship among various modalities, can be used to register the acquired datasets, independently of the imaged object. The transformation matrix is easily obtained using the calibration phantom and the holder. The calibration procedure is automatic and requires no user interaction. The method is simple and does not depend on any preparation and postprocessing. It is appropriate for routine fusion studies with mass scanning.

Acknowledgment

The authors would like to thank C.-H. Yeh for his assistance with the data acquisitions of CT and SPECT; and Dr. W. Lin and C.-S. Shyu for their help with the [^{18}F]-FDG preparation.

References

[1] S. R. Cherry and S. Gambhir, "Use of positron emission tomography in animal research," *Inst. Lab. Animal Res. J.*, vol. 42, pp. 219–232, 2001.
[2] D. L. G. Hill, P. G. Batchelor, M. Holden, and D. J. Hawkes, "Medical image registration," *Phys. Med. Biol.*, vol. 46, p. R1-45, 2001.
[3] M. W. Wilson and J. M. Mountz, "A reference system for neuroanatomical localization on functional reconstructed cerebral images," *J. Comput. Assist. Tomogr.*, vol. 13, pp. 174–178, 1989.
[4] R. L. Phillips, E. D. London, J. M. Links, and N. G. Cascella, "Program for PET image alignment: effect of calculated differences in cerebral metabolic rates for glucose," *J. Nucl. Med.*, vol. 31, pp. 2052–2057, 1990.
[5] L. R. Schad, R. Boesecke, W. Schilegel, G. H. Hartmann, V. Sturm, L. G. Strauss, and W. J. Lorenz, "Three dimensional image correlation of CT, MR and PET studies in radiotherapy planning of brain tumors," *J. Comput. Assist. Tomogr.*, vol. 11, pp. 948–954, 1987.
[6] M. L. J. Apuzzo, P. T. Chandirasoma, D. Cohen, C. S. Zee, and V. Zelman, "Computed imaging stereotaxy: experience and perspective related to 500 procedures applied to brain masses," *Neurosurgery*, vol. 20, pp. 930–937, 1987.
[7] J. Zhang, M. F. Levesque, C. L. Wilson, R. M. Harper, J. Engel, R. Lufkin, and E. J. Behnke, "Multimodality imaging of brain structures for stereotactic surgery," *Radiology*, vol. 175, pp. 435–441, 1990.
[8] D. L. G. Hill, D. J. Hawkes, J. E. Crossman, M. J. Gleeson, T. C. S. Cox, and L. Bracey *et al.*, "Registration of MR and CT images for skull base surgery using point-like anatomical features," *Br. J. Radiol.*, vol. 64, pp. 1030–1035, 1991.
[9] N. Hayakawa, K. Uemura, K. Ishiwata, Y. Shimada, N. Ogi, and T. Nagaoka *et al.*, "A PET-MRI registration technique for PET studies of the rat brain," *Nucl. Med. Biol.*, vol. 27, pp. 121–125, 2000.
[10] D. Stout, P. Chow, B. Silverman, R. Leahy, X. Lewis, S. Gambhir, and A. Chatziioannou, "Creating a whole body digital mouse atlas with PET, CT and cryosection images," presented at the *AMI Ann. Conf.*, San Diego, CA, Oct. 23–27, 2002.
[11] J. J. Vaquero, M. Desco, J. Pascau, A. Santos, I. Lee, J. Seidel, and M. V. Green, "PET, CT, and MR image registration of the rat brain and skull," *IEEE Trans. Nucl. Sci.*, vol. 48, no. 4, pp. 1440–1445, Aug. 2001.
[12] L. A. Feldkamp, L. C. Davis, and J. W. Kress, "Practical cone-beam algorithm," *J. Opt. Soc. Am. A*, vol. 1, pp. 612–619, 1984.
[13] K. Iwata, B. E. Patt, J. Li, K. B. Parnham, T. Vandehei, and J. S. Iwanczyk *et al.*, "Dedicated small animal MicroSPECT/CT system with stationary horizontal animal position," presented at the *IEEE NSS-MIC*, Portland, OR, Oct. 19–25, 2003.
[14] C. Knoess, S. Siegel, A. Smith, D. Newport, N. Richerzhagen, and A. Winkeler *et al.*, "Performance evaluation of the microPET R4 PET scanner for rodents," *Eur. J. Nucl. Med. Mol. Imag.*, vol. 30, pp. 737–747, 2003.
[15] P. E. Kinahan and J. G. Rogers, "Analytic three-dimensional image reconstruction using all detected event," *IEEE Trans. Nucl. Sci.*, vol. 36, no. 1, pp. 964–968, Feb. 1989.
[16] B. D. Smith, "Image reconstruction from cone-beam projection: necessary and sufficient conditions and reconstruction methods," *IEEE Trans. Med. Imag.*, vol. MI-4, pp. 14–25, 1985.